ACS Catalysis

Research Article

pubs.acs.org/acscatalysis

Structure Sensitivity of $La_2O_2CO_3$ Catalysts in the Oxidative Coupling of Methane

Yu-Hui Hou, Wei-Chen Han, Wen-Sheng Xia,* and Hui-Lin Wan*

State Key Laboratory of Physical Chemistry of Solid State Surfaces, National Engineering Laboratory for Green Chemical Productions of Alcohols-Ethers-Esters, Fujian Province Key Laboratory of Theoretical and Computational Chemistry, College of Chemistry and Chemical Engineering, Xiamen University, Xiamen, Fujian 361005, P. R. China

Supporting Information

ABSTRACT: Methane is the main component of natural gas and shale gas. It is chemically stable, and its activation often requires high temperatures, which lead to its extensive transformation into undesirable products such as CO and CO_2. Thus, the development of efficient catalysts for the selective transformation of methane represents a substantial challenge. In this work, we synthesized $La_2O_2CO_3$ samples with different morphologies (rod- and plate-shapes) at the nanometer scale. We observed that one of the rod-shaped samples exhibited the best catalytic properties among the investigated samples in the oxidative coupling of methane (OCM) at low temperatures (420−500 °C); in addition, its specific activity was 20 times greater than that of any of the other rod-shaped samples. This difference corresponded to the O_2-TPD results and was attributed to the crystallographic facets exposed. Among the exposed facets, the (110), (1$\bar{2}$0), and (2$\bar{1}$0) facets had relatively loose atomic configurations that increased the conversion of methane in the OCM. Moreover, these facets were beneficial to the formation of the chemisorbed oxygen species and their moderately basic sites, which improve the selectivity in the OCM.

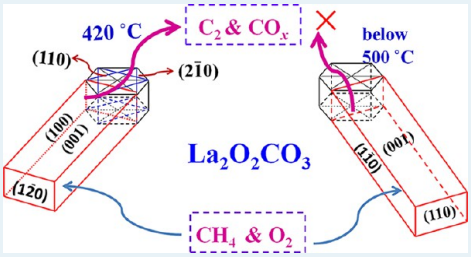

KEYWORDS: *lanthanum oxycarbonate, morphology, structure sensitivity, oxidative coupling of methane, low temperature*

1. INTRODUCTION

Heterogeneous catalysis processes include the adsorption and transformation of reaction molecules and the desorption of products. This process involves the breakage and formation of chemical bonds and is strongly dependent on the atomic arrangement on the surface of the catalyst,[1−6] which means that the catalytic properties (activity and selectivity) of the solid particles could be intimately linked with the exposed crystallographic facets. The formation rate of ammonia from N_2 and H_2 on an Fe crystal decreases according to the order (111) ≫ (100) > (110).[7] Tetrahexahedral Pt nanocrystals encircled by high-index (730), (210), and (520) facets have been reported to exhibit greater atomic step edges and dangling bond densities and were observed to be more active in the electro-oxidation of light oxygenates than octahedral Pt nanoparticles with exposed low-index (111), (100), and (110) planes.[8] Octahedral Pt with more exposed (111) terraces exhibited much higher enantioselectivity than other forms of similar sized Pt particles with fewer exposed (111) facets.[9] Moreover, some examples that support the correlation of the catalytic properties of metal oxides with the exposed crystallographic facets have been reported in the literature. MoO_3 showed catalytic anisotropy during propylene oxidation, with greater acrolein selectivity for the (100) plane and complete oxidation to CO_2 on the (010) facets.[10] CeO_2 nanorods with exposed (110) and (100) facets have been shown to be generally more active toward CO oxidation than cubic particles with exposed (100) facets and octahedral particles with exposed (111) facets.[11−14]

However, the literature contains few reports regarding the correlation of catalytic activity in the oxidative coupling of methane (OCM) with the crystallographic facets of the catalysts. This correlation involves the nature of the reaction and the catalysts. Like most of the important reactions of methane, OCM has been a desirable but still inefficient route for methane utilization because methane is chemically inert (with high C−H bond strengths, a negligible electron affinity, a large ionization energy, and a low polarizability); its activation therefore often requires high temperatures, which lead to the extensive transformation of the targeted products (C2+ compounds). Thus, achieving kinetic control over the selective transformation of methane is very difficult. Furthermore, OCM catalysts are generally metal oxides that are commonly prepared via the precipitation of metal salts from an aqueous phase followed by high-temperature calcination (at a temperature higher than that required for conversion of methane); consequently, sphere-shaped particles tend to be produced. Recently, catalysts (metal oxides) at the nanometer scale have been observed to activate methane at lower temperatures.[2,15−21] For instance, Senkan[21] reported that La_2O_3−CeO_2 nanofibers exhibited OCM ignition at 470 °C (with a CH_4/O_2 ratio of 7 and a gas hourly space velocity (GHSV) of 900 × 10^3 mL·g^{-1}·h^{-1}), resulting in an 18% yield of C2+ compounds and a 65% C2+ selectivity at 520 °C.

Received: November 4, 2014
Revised: January 30, 2015
Published: February 2, 2015

DOI: 10.1021/cs501733r
ACS Catal. 2015, 5, 1663−1674

Thus, well-defined catalysts at the nanometer scale can be prepared via calcination at low temperatures and then used for OCM.

Many researchers have demonstrated that lanthanum-based catalysts are efficient in OCM.[2,21−29] Notably, Au[29] reported that the presence of the $La_2O_2CO_3$ phase appeared to have a beneficial effect on the catalytic performance, and Schrader[28] reported that the catalytic activity of the $La_2O_2CO_3$ catalysts was better than that of La_2O_3. Thus, $La_2O_2CO_3$ as a catalyst for OCM is a good candidate for study at the nanometer scale.

In the present work, we focused on the synthesis of $La_2O_2CO_3$ with a well-defined nanostructure and explored the effects of its exposed crystallographic facets or morphologies on its catalytic properties in the OCM.

2. EXPERIMENTAL SECTION

2.1. Catalyst Preparation. *2.1.1. Synthesis of $La_2O_2CO_3$ Using a Hydrothermal Method.* In a typical synthesis, 1.0000 g of $La(NO_3)_3{\cdot}6H_2O$ was added to 50.0 mL of deionized water, and the resulting solution was stirred vigorously to ensure complete dissolution. The pH of the solution was adjusted to 11.5 with 10 wt % NaOH solution, yielding a white precipitate after the mixture was stirred for approximately 10 min. Subsequently, the solution was transferred to an autoclave (100 mL), heated to 160 °C and maintained at this temperature for 12 h. The obtained product was centrifuged, and the separated precipitate was washed with distilled water and ethanol and then dried at 90 °C to give $La(OH)_3$. This sample was transformed into $La_2O_2CO_3$ when calcined in air at 500 °C for 2 h (or into La_2O_3 when calcined in air at 700 °C for 2 h).

For comparison, $La_2O_2CO_3$ was also synthesized using a hydrothermal method based on the procedure reported by Shen.[30]

2.1.2. Synthesis of $La_2O_2CO_3$ Using a Precipitation Method. In a typical synthesis, 1.0000 g of $La(NO_3)_3{\cdot}6H_2O$ was added to 50.0 mL of deionized water, and the resulting solution was stirred vigorously to ensure complete dissolution. The pH of the solution was adjusted to 11.5 with 10 wt % NaOH solution, yielding a white precipitate after the mixture was stirred for approximately 10 min. The sample was continuously stirred for another 12 h, and the obtained product was centrifuged. The separated precipitate was washed with distilled water and ethanol and then dried at 90 °C to give $La(OH)_3$. This sample was converted into $La_2O_2CO_3$ by calcination in air at 500 °C for 2 h (or into La_2O_3 by calcination in air at 700 °C for 2 h).

For simplicity, we labeled the reference $La_2O_2CO_3$ sample as $La_2O_2CO_3{-}H_{ref}$ and denoted the $La_2O_2CO_3$ samples synthesized by the hydrothermal and precipitation methods as $La_2O_2CO_3{-}H$ and $La_2O_2CO_3{-}P$, respectively. Likewise, we labeled the pertinent samples of $La(OH)_3$ as $La(OH)_3{-}H$ (or H_{ref}) and $La(OH)_3{-}P$ and denoted the relevant samples of La_2O_3 as $La_2O_3{-}H$ (or H_{ref}) and $La_2O_3{-}P$.

2.2. Catalyst Characterization. Thermogravimetric (TG) analysis and differential thermal analysis (DTA) were performed in air on an SDT-Q600 apparatus (New Castle, DE, U.S.A). The precalcined samples were heated from 10 to 1000 °C under a flowing air stream at a heating rate of 10 °C·min^{-1}. The air flow rate was 100 mL·min^{-1}.

X-ray powder diffraction (XRD) analysis was carried out on a Panalytical X'pert PRO diffractometer (The Netherlands). The samples were scanned from 10 to 90° 2θ. Cu Kα radiation (λ = 0.15406 nm) generated at 40 kV and 30 mA was used as the X-ray source.

Fourier-transform infrared (FT-IR) spectra of the samples in the form of KBr pellets were recorded at room temperature on a Bruker Vector 33 microscope (Billerica, MA, U.S.A.) equipped with a Gatan 832 CCD camera.

The surface areas of the samples were determined from the N_2 adsorption and desorption isotherms at −196 °C using a multipoint BET equation on an automated Micromeritics Tristar 3000 apparatus (Norcross, GA, U.S.A.). The samples were outgassed for 3 h under vacuum at 300 °C before the measurements were performed.

The scanning electron microscopy (SEM) characterization of the samples was performed on a Hitachi S-4800 FEGSEM microscope (Japan) at an acceleration voltage of 15 kV. The transmission electron microscopy (TEM) and the high-resolution transmission electron microscopy (HRTEM) characterizations of the samples were performed on a Tecnai F-30 electron microscope (The Netherlands) operated at an acceleration voltage of 300 kV. The selected-area electron diffraction (SAED) data were collected on a Tecnai F-20 instrument (The Netherlands) operated at an acceleration voltage of 200 kV.

The CO_2 temperature-programmed desorption (CO_2-TPD) analyses of the samples were carried out in a gas flow system equipped with a mass analyzer HIDEN QIC-20 (U.K.). Each sample (0.1000 g) was calcined at 500 °C under a helium atmosphere for 1 h, cooled to 50 °C, and exposed to pure CO_2 for 1 h at 50 °C. After the sample chamber was purged with helium for 1 h at 50 °C to ensure a flat baseline, the TPD plot was obtained at a heating rate of 10 °C·min^{-1} to 900 °C. (A similar treatment was used for the O_2 temperature-programmed desorption (O_2-TPD), except that the desorption temperature ranged from 40 to 800 °C.) To quantify the rate of CO_2 (or O_2) desorption from the surface of the catalyst, 20%CO_2/He (or 20% O_2/He) (0.7 mL) was used as the adsorbate gas to determine the correlation between the quantity of CO_2 (or O_2) desorbed from the surface and the areas of the TPD peaks.

The TPD-MS analyses of the samples were carried out in a gas flow system equipped with a mass analyzer. The precalcined samples (0.1000 g) were heated from room temperature to 800 °C in a flowing 20%O_2/He mixture at a heating rate of 10 °C·min^{-1}. The flow rate of the 20%O_2/He mixture was 60 mL·min^{-1}.

X-ray photoelectron spectroscopy (XPS) experiments were performed using an Omicron Sphera II hemispherical electron energy analyzer (U.K.) at a base pressure of 5.0×10^{-9} mbar; the instrument was equipped with a monochromatic Al Kα radiation source operated at a power of 300 W. The spectra were corrected using the C 1s signal located at 284.5 eV. The O 1s envelopes were deconvoluted into the contributions of the corresponding surface oxygen species using the software XPS-peak. For all of the computer fits, the XPS peaks were assumed to have 80% Gaussian and 20% Lorentzian peak shapes. The correctness of the analysis method was verified by deconvolution of a simulated peak composed of four single peaks with known binding energies and peak widths.

2.3. Catalyst Testing. The catalytic performances of the samples were investigated using a mixture of methane and oxygen (CH_4/O_2 = 3/1 molar ratio) as the reaction feed. The OCM reaction was carried out in a fixed-bed quartz tubular reactor (internal diameter 5 mm) at atmospheric pressure and at a total flow rate of 50 mL·min^{-1}. The reactor was packed with 0.1000 g of the investigated sample (40−60 mesh sizes) between quartz wool plugs and was heated with a furnace connected to a

DOI: 10.1021/cs501733r
ACS Catal. 2015, 5, 1663−1674

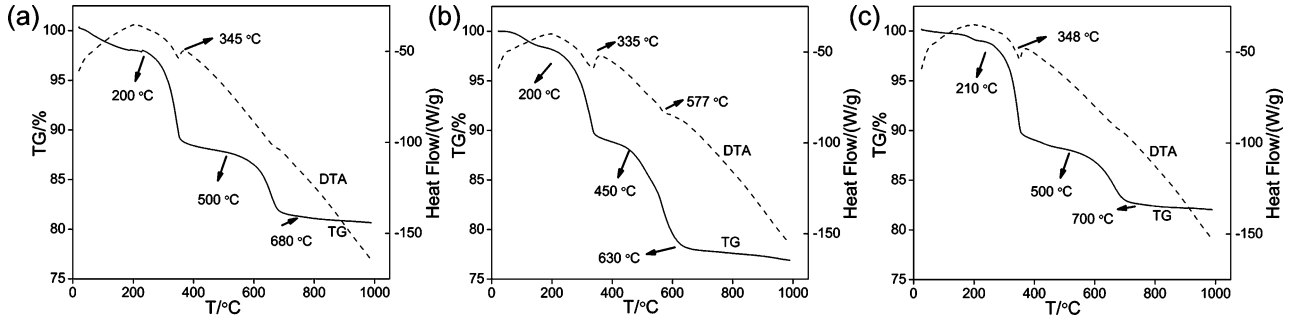

Figure 1. TG and DTA curves of the samples: (a) $La(OH)_3$–H, (b) $La(OH)_3$–P, and (c) $La(OH)_3$–H_{ref}.

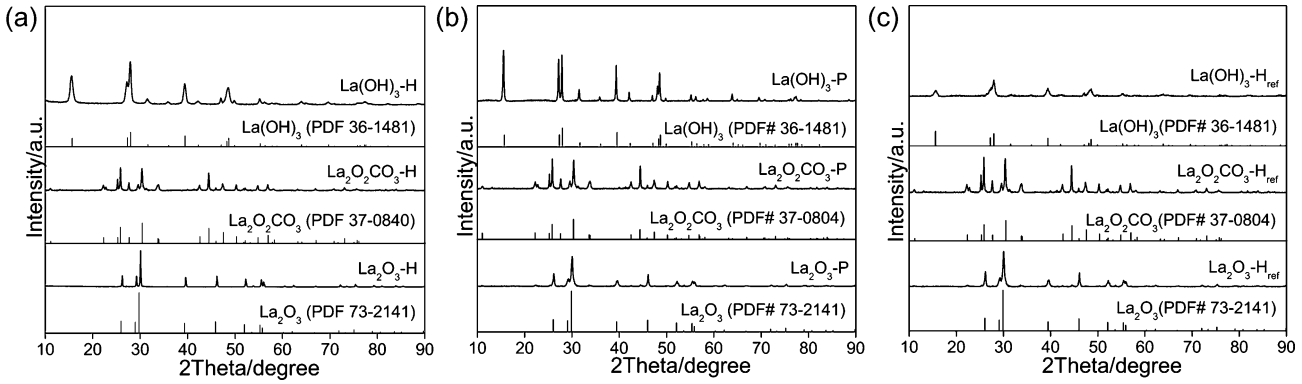

Figure 2. XRD patterns of $La(OH)_3$, $La_2O_2CO_3$ and La_2O_3.

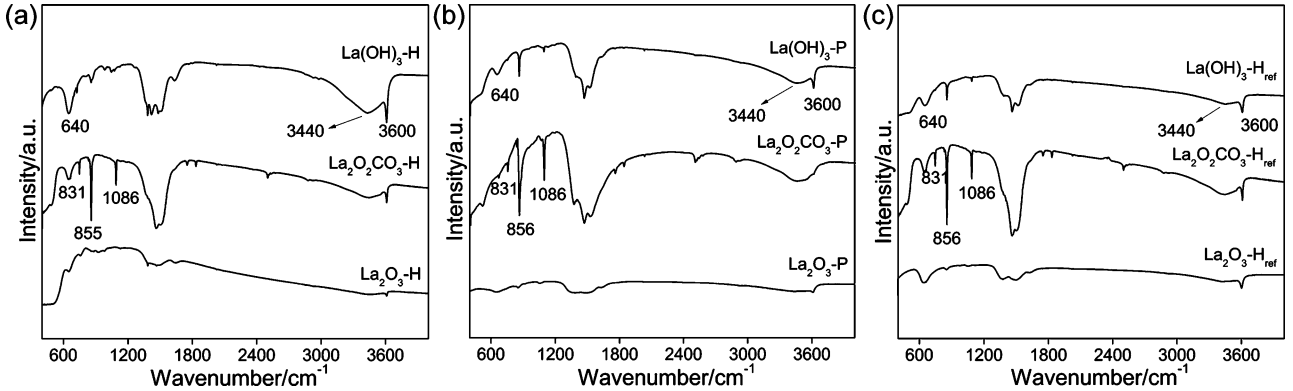

Figure 3. FT-IR spectra of the $La(OH)_3$ samples and the calcined samples ($La_2O_2CO_3$, La_2O_3).

temperature controller (Yudian AI-708PFKSL2). The performances of the catalysts were evaluated over the temperature range of 400–500 °C, with a GHSV of 30 000 $mL \cdot g^{-1} \cdot h^{-1}$. Quartz sand was also tested in the reactor as a blank, which confirmed that the homogeneous conversion of CH_4 started from $T > 800$ °C. The data analysis method was the same as that used in our previous report.[27]

3. RESULTS AND DISCUSSION

3.1. Phase Changes of $La(OH)_3$ under Thermal Treatments. Bernal[31,32] and Mu[33,34] reported that the presence of CO_3^{2-} and $OHCO_3^{3-}$ was detected when the lanthanum hydroxide was heated in air—that is, the lanthanum hydroxide might have transformed into carbonate or hydroxycarbonate when heated in air. To analyze the decomposition process of the synthesized $La(OH)_3$–H, $La(OH)_3$–P, and $La(OH)_3$–H_{ref} samples and to understand the changes that occurred in the samples during calcination in air, TG and DTA measurements were carried out under a flowing air atmosphere. As shown in Figure 1, the changes in the samples at elevated temperatures can be summarized as occurring in three steps: the first step occurred at temperatures ranging from room temperature to ~200 °C; the second step occurred at ~200 to ~500 °C; and the third step occurred at ~500 to 800 °C. According to the TPD-MS study shown in Figure S1 (Supporting Information (SI)), the TG traces (Figure 1) showed that water was the only product emitted during the first two steps, whereas CO_2 was generated exclusively during the third step. Thus, the first weight loss (~2%) was attributed to the removal of water adsorbed onto the surface of the $La(OH)_3$ samples; the second weight loss (~10%) was due to the removal of water during the conversion of hydroxycarbonate into $La_2O_2CO_3$; and the third weight loss (~7% or ~12%) was ascribed to the conversion of $La_2O_2CO_3$ to La_2O_3.[31,32,34,35] These arguments are supported by the subsequent XRD and FT-IR results.

DOI: 10.1021/cs501733r
ACS Catal. 2015, 5, 1663–1674

Figure 2 shows the XRD patterns of the samples before and after calcination. The three precalcined samples ($La(OH)_3$−H_{ref}, $La(OH)_3$−H, and $La(OH)_3$−P) exhibited characteristic diffraction peaks that matched the hexagonal lanthanum hydroxide phase (PDF 36-1481) (no hydroxycarbonate was identified, revealing that bulk carbonation did not occur); however, the patterns of the calcined samples showed different characteristic peaks from $La(OH)_3$. The characteristic diffraction peaks of the samples calcined in air at 500 °C for 2 h matched those of the hexagonal $La_2O_2CO_3$ phase (PDF 37-0804), and those of samples calcined in air at 700 °C for 2 h corresponded to the hexagonal phase of La_2O_3 (PDF 73-2141). The XRD patterns of all three $La(OH)_3$ samples ($La(OH)_3$−H_{ref}, $La(OH)_3$−H, and $La(OH)_3$−P) synthesized by different methods were similar to each other, either did the related $La_2O_2CO_3$ and La_2O_3 samples.

Moreover, the three samples with the same composition synthesized by different methods exhibited similar FT-IR spectra (Figure 3). The IR adsorption bands at 3600 and 640 cm^{-1} were associated with the OH stretching[36] and La−OH bending[37] modes in lanthanum hydroxide, and the bands at 3440 cm^{-1} and between 1200 and 1600 cm^{-1} in the spectra of all of the samples (Figure 3a−c) revealed the existence of a hydroxycarbonate phase.[31,35] These results indicated that these samples have a high capacity for adsorbing CO_2 and H_2O, especially the precalcined and postcalcined samples (at 500 °C). In addition, the two main vibration peaks of the calcined samples (at 500 °C) at 856 and 1086 cm^{-1} were attributed to the ν_2 and ν_1 modes of $La_2O_2CO_3$.[38] The peak at 831 cm^{-1} was ascribed to the carbonate groups originating from the reaction of the samples with CO_2 in air.[39]

In summary, the aforementioned results suggest that $La(OH)_3$, which has a high capacity for adsorbing CO_2 and H_2O, was transformed into $La_2O_2CO_3$ via an intermediate hydroxycarbonate at 200−500 °C when heated in air and that the formed $La_2O_2CO_3$ was further converted into La_2O_3 at 500−800 °C. Thus, on the basis of the weight loss of the samples in the TG traces (Figure 1) combined with the XRD and IR analyses (Figures 2 and 3), we propose a possible pathway for the decomposition of $La(OH)_3$ in Scheme 1.

Scheme 1. Possible Pathway for the Formation/Decomposition of $La_2O_2CO_3$ When $La(OH)_3$ Is Heated in Air

$$2La(OH)_3 + CO_2 + H_2O \rightarrow La_2(OH)_{6-2x}(CO_3)_x \cdot \delta H_2O \xrightarrow[-H_2O]{1st\ step} La_2(OH)_{6-2x}(CO_3)_x \xrightarrow[-H_2O]{2nd\ step} La_2O_2CO_3 \xrightarrow[-CO_2]{3rd\ step} La_2O_3$$

where $x \simeq 1$

This scheme is consistent with those reported in the literature.[33−35] Consequently, the synthesized samples of $La(OH)_3$ are reasonably assumed to have been completely transformed into $La_2O_2CO_3$ via calcination in air at 500 °C for 2 h and into La_2O_3 via calcination in air at 700 °C for 2 h.

3.2. Physicochemical Properties of $La_2O_2CO_3$. The SEM images of the $La(OH)_3$, $La_2O_2CO_3$ and La_2O_3 samples are shown in Figure 4. The samples synthesized using a hydrothermal method appeared to be rod-shaped (Figure 4a−c and Figure 4g−i), and those synthesized using a precipitation method appeared to be plate-shaped (Figure 4d−f). The size distribution of the rod-shaped sample was obviously more uniform than that of the plate-shaped sample (Figure S2 (SI)). The average sizes of the samples are listed in Table 1. Specifically, the rod-shaped $La_2O_2CO_3$−H sample (diameter: 19.1 ± 2.2 nm, length: 185.7 ± 13.6 nm) was prepared via the calcination of $La(OH)_3$−H (diameter: 15.1 ± 1.8 nm, length: 187.7 ± 12.1 nm) in air at 500 °C for 2 h. Both the rod-shaped $La_2O_2CO_3$−H sample and the rod-shaped $La(OH)_3$−H sample were similar in size to the La_2O_3−H sample (diameter: 19.6 ± 2.4 nm, length: 192.7 ± 13.9 nm), which was prepared via the calcination of $La(OH)_3$−H in air at 700 °C for 2 h. Similarly, the rod-shaped $La(OH)_3$−H_{ref}, $La_2O_2CO_3$−H_{ref} and La_2O_3−H_{ref} samples were comparable in size (diameter: ∼15−20 nm, length: ∼300 nm). However, the particles in these three samples were significantly longer than those in the $La(OH)_3$−H, $La_2O_2CO_3$−H and La_2O_3−H samples. Furthermore, the plate-shaped $La(OH)_3$−P, $La_2O_2CO_3$−P and La_2O_3−P samples were shown to have similar sizes (diameter: ∼20−100 nm; thickness: ∼10−25 nm). Thus, the morphologies (rod-shaped or plate-shaped) of the samples calcined at the lower temperatures were well maintained.

The sizes and pore parameters of the samples are shown in Table 1. For $La(OH)_3$, $La_2O_2CO_3$, and La_2O_3, the diameters of the samples were slightly increased, and the pore diameters, the pore volume, and the specific surface areas of the samples were decreased. These results indicated that the structures of these porous samples exhibited some shrinkage upon calcination, although the $La_2O_2CO_3$ sample did not contract as much as the La_2O_3 sample. Actually, the pore parameters of the $La_2O_2CO_3$ sample were very similar to those of the $La(OH)_3$ sample.

By comparing the rod-shaped and plate-shaped $La_2O_2CO_3$ samples (Table 1), we noted that the diameter of the plate-shaped sample was greater than that of the rod-shaped sample (∼30−100 vs ∼20 nm), whereas the specific surface area and pore volume of the plate-shaped $La_2O_2CO_3$ sample were significantly less than those of the rod-shaped sample (∼10 vs ∼70 $m^2 \cdot g^{-1}$; 0.02 vs ∼0.16 $m^3 \cdot g^{-1}$). Their pore diameters were approximately the same (∼12 vs ∼11 nm). Similar results were obtained from a comparison of the shapes of the $La(OH)_3$ and La_2O_3 samples. These findings suggest that the dispersion of the rod-shaped $La_2O_2CO_3$ sample was better than that of the plate-shaped sample.

3.3. Catalytic Performances of $La_2O_2CO_3$. The catalytic performances of the samples were tested for the OCM reaction; some data at selected temperatures are listed in Table 2. We note that a blank tube loaded with quartz sand exhibited only 0.6% conversion of methane without C2 products at 650 °C, indicating that the homogeneous conversion of methane to C2 hydrocarbons is ignored. Over the rod-shaped $La_2O_2CO_3$−H nanoparticles at 420 °C, the conversion of methane was approximately 30% and the C2 selectivity was approximately 50%; however, over the plate-shaped $La_2O_2CO_3$−P nanoparticles at 420 °C, no methane was converted (conversions of methane greater than 10% can only occur at 500 °C and above). This result indicates the significant effects of the morphology of the catalyst on its activity. Moreover, the conversion of methane and C2 selectivity over the rod-shaped $La_2O_2CO_3$−H nanoparticles were almost unchanged at temperatures ranging from 420 to 500 °C, indicating good stability of the $La_2O_2CO_3$−H catalyst during OCM. The conversion of oxygen over the $La_2O_2CO_3$−H catalyst was greater than that over $La_2O_2CO_3$−P at 420−500 °C, indicating that $La_2O_2CO_3$−H exhibited a higher capacity to activate or replenish oxygen at lower temperatures.

DOI: 10.1021/cs501733r
ACS Catal. 2015, 5, 1663−1674

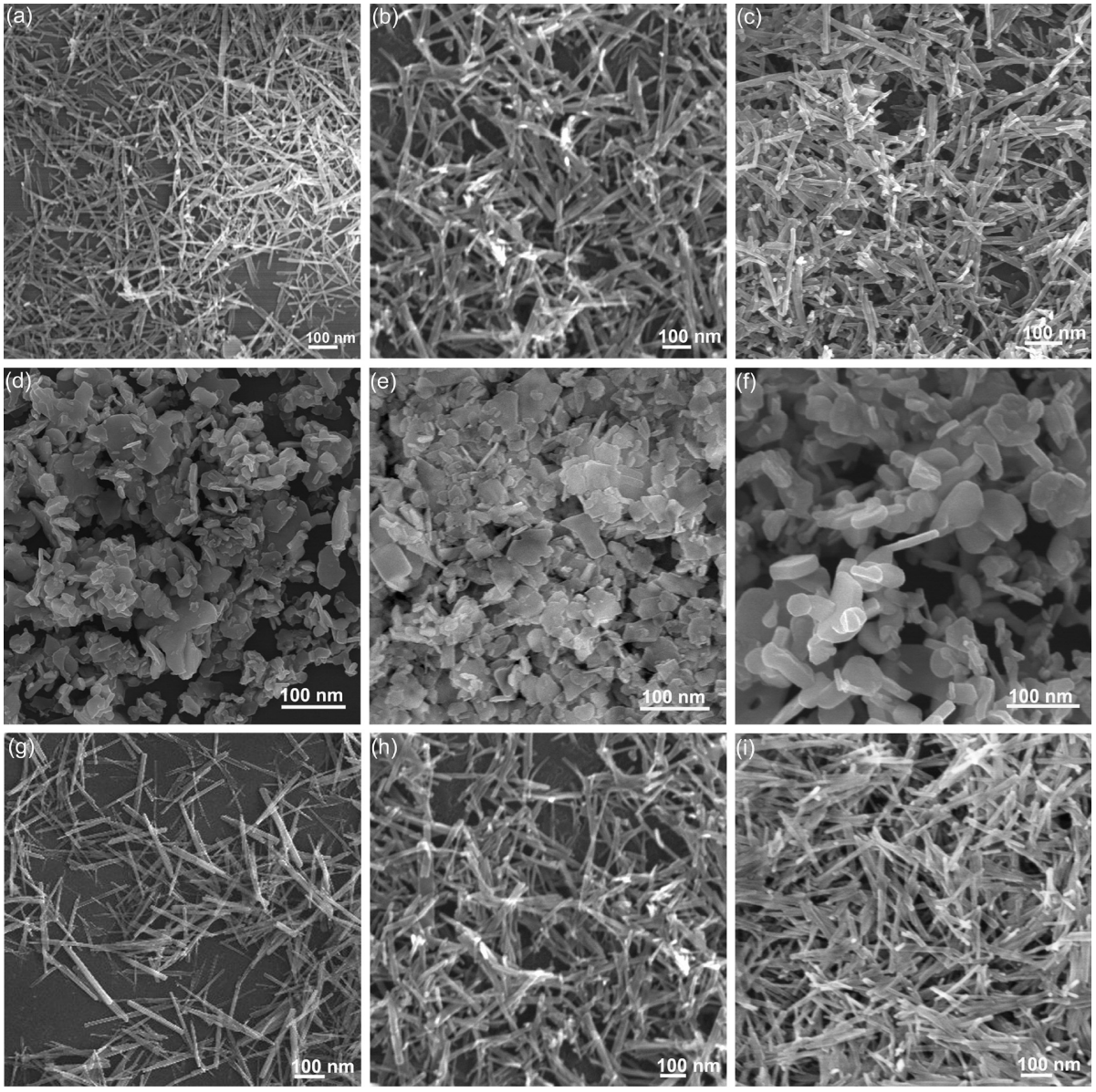

Figure 4. SEM images of the samples: (a) $La(OH)_3$–H, (b) $La_2O_2CO_3$–H, (c) La_2O_3–H, (d) $La(OH)_3$–P, (e) $La_2O_2CO_3$–P, (f) La_2O_3–P, (g) $La(OH)_3$–H_{ref}, (h) $La_2O_2CO_3$–H_{ref}, and (i) La_2O_3–H_{ref}.

Table 1. Physicochemical Properties of the Samples

topography	samples	$S_{BET}/m^2 \cdot g^{-1}$	D_p/nm	$V_p/m^3 \cdot g^{-1}$	D_{SEM}/nm	L_{SEM} or T_{SEM}/nm
rod	$La(OH)_3$–H	70.2	12.4	0.19	15.1 ± 1.8	187.7 ± 12.1
	$La_2O_2CO_3$–H	68.6	11.8	0.16	19.1 ± 2.2	185.7 ± 13.6
	La_2O_3–H	16.8	7.7	0.05	19.6 ± 2.4	192.7 ± 13.9
plate	$La(OH)_3$–P	13.6	11.2	0.03	20–100	11.7 ± 1.1
	$La_2O_2CO_3$–P	12.2	10.8	0.02	30–100	14.2 ± 1.8
	La_2O_3–P	6.0	7.2	0.01	50–100	24.3 ± 1.8
rod	$La(OH)_3$–H_{ref}	73.0	13.1	0.19	15.1 ± 1.6	292.9 ± 1.9
	$La_2O_2CO_3$–H_{ref}	71.2	12.0	0.17	20.0 ± 2.1	288.9 ± 18.5
	La_2O_3–H_{ref}	18.0	8.1	0.03	18.1 ± 1.6	288.2 ± 18.1

S_{BET}, D_p, V_p stand for specific surface areas, porous diameters, porous volume of the samples, respectively; D_{SEM}, L_{SEM}, or T_{SEM} represent diameters, lengths, or thickness of the samples by SEM, respectively.

3.3.1. O_2-TPD Characterization. O_2-TPD profiles are usually used to measure the ability of a catalyst to activate oxygen and to measure its oxygen storage capacity (OSC). As shown in Figure 5, two distinct desorption peaks of oxygen from $La_2O_2CO_3$–H were observed, at 320 and 524 °C. The former was attributed to molecular oxygen species (200–400 °C), and the latter was ascribed to chemisorbed oxygen species (400–600 °C).[40] As a comparison, the desorption peak of oxygen from $La_2O_2CO_3$–P

DOI: 10.1021/cs501733r
ACS Catal. 2015, 5, 1663–1674

Table 2. Catalytic Performances of $La_2O_2CO_3$ for OCM

catalysts	T/°C	conv CH_4/%	conv O_2/%	sel CO_x/%	sel C2/%	Y C2/%
$La_2O_2CO_3$–H	410	8.3	30.2	100.0	0.0	0.0
	420	29.7	95.1	51.6	48.4	14.4
	420[a]	27.6	90.3	50.7	49.3	13.6
	440	30.0	97.2	51.0	49.0	14.7
	450	30.2	99.3	51.5	48.5	14.7
	500	30.5	99.8	51.4	48.6	14.8
$La_2O_2CO_3$–P	410	0.0	0.0	100.0	0.0	0.0
	420	0.0	0.0	100.0	0.0	0.0
	440	0.3	0.8	100.0	0.0	0.0
	450	1.5	5.1	100.0	0.0	0.0
	500	26.8	92.0	71.9	29.1	7.8
$La_2O_2CO_3$–H_{ref}	450	0.0	0.0	0.0	0.0	0.0
	500	1.5	0.0	0.0	0.0	0.0
La_2O_3–H	420	5.4	14.5	100.0	0.0	0.0
	450[b]	26.2(12.9)	93.6(36.8)	58.5(74.2)	41.5(25.8)	10.9(3.3)
	500[b]	27.4(25.4)	97.3(93.0)	56.6(75.7)	43.4(24.3)	11.9(6.2)
La_2O_3–P	450	2.3	7.9	100.0	0.0	0.0
	500	16.2	64.3	75.4	24.6	4.0
La_2O_3–H_{ref}	450	0.0	0.0	0.0	0.0	0.0
	500	1.2	4.8	100.0	0.0	0.0
blank	650	0.6	2.5	100.0	0.0	0.0

[a]Just for $La_2O_2CO_3$ prepared via water-treated La_2O_3 followed by desiccation and calcination; [b]The data in the parentheses were collected in the case that the reactant gases were switched into the reactor loaded with the fresh catalyst at the selected temperature; Conv: Conversion; Sel: Selectivity; Y: Yield.

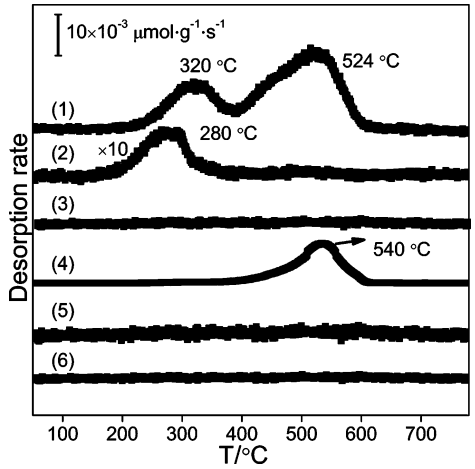

Figure 5. O_2-TPD curves of the samples: (1) $La_2O_2CO_3$–H, (2) $La_2O_2CO_3$–P, (3) $La_2O_2CO_3$–H_{ref}, (4) La_2O_3–H, (5) La_2O_3–P, and (6) La_2O_3–H_{ref}.

was located at 280 °C (molecular oxygen species), which is lower than desorption peak temperature of oxygen from $La_2O_2CO_3$–H, and its peak area is far less than that from $La_2O_2CO_3$–H (corresponding densities of sites for O_2 adsorption: 0.03 vs 0.52 μmol·m^{-2}, Table S1 (SI)). These data suggest that $La_2O_2CO_3$–H is a stronger oxygen activator with a far larger OSC than $La_2O_2CO_3$–P, which is beneficial to the activation and replenishment of oxygen.

Notably, in terms of oxygen adsorption, large quantities of chemisorbed oxygen species and molecular oxygen species were present over the $La_2O_2CO_3$–H catalyst, whereas just a few molecular oxygen species were present over the $La_2O_2CO_3$–P catalyst (Figure 5, Table S1 (SI)). High C2 selectivity (~48%) was observed over $La_2O_2CO_3$–H, and almost no C2 was detected over $La_2O_2CO_3$–P when methane oxidation occurred at lower temperatures (<500 °C) (Table 2). Additionally, over La_2O_3–H, only chemisorbed oxygen species (540 °C) for oxygen adsorption and significant C2 products for methane oxidation were observed at temperatures above 450 °C. Moreover, we observed no oxygen species to indicate oxygen adsorption (Figure 5, Table S1 (SI)) and no C2 products to indicate methane oxidation over $La_2O_2CO_3$–H_{ref}, La_2O_3–H_{ref}, and La_2O_3–P at lower temperatures (<500 °C) (Table 2). These findings reveal that gaseous oxygen or molecular oxygen species are related to the deep oxidation of methane and that chemisorbed oxygen species are linked to the selective oxidation of methane; these results are in good agreement with the results of previous reports.[41,42]

The chemisorbed oxygen species may have been O_2^{2-}, O_2^-, O^-, and O^{2-}, which arise from the interaction of oxygen with catalysts. Each of these oxygen species may exist in equilibrium, depending on the nature of the catalyst.[43−46] The electron-deficient oxygen species (O^- and O_2^{2-}) on the catalyst surfaces effectively improve the C2 selectivity,[41,42,47] whereas lattice oxygen (O^{2-}) is reportedly responsible for complete oxidation.[47,48] Figure S3 (SI) shows the XPS characterization of the $La_2O_2CO_3$–H, $La_2O_2CO_3$–P, and $La_2O_2CO_3$–H_{ref} samples. Four different oxygen species were observed from the O 1s spectra of $La_2O_2CO_3$–H, $La_2O_2CO_3$–P, and $La_2O_2CO_3$–H_{ref}. These species were assigned to CO_3^{2-} at 531.5−532.5 eV, O_2^{2-} at 530.5−531.1 eV, O^- at 530.1−530.2 eV, and O^{2-} at 528.0−529.0 eV.[49−52] The relative values of the peak areas of these oxygen species are summarized in Table S2 (SI). Using these data, we estimated the ratio of surface electrophilic oxygen (O_2^{2-} and O^-) to lattice oxygen (O^{2-}) species from the relative amounts of the oxygen species calculated according to the areas under each peak. The results in Table S2 (SI) show that the ratio $(O_2^{2-}+O^-)/O^{2-}$ was greater on the surface of the $La_2O_2CO_3$–H sample than on the $La_2O_2CO_3$–H_{ref} and $La_2O_2CO_3$–P samples,

DOI: 10.1021/cs501733r
ACS Catal. 2015, 5, 1663−1674

demonstrating that the chemisorbed oxygen species (electrophilic oxygen) were responsible for the C2 selectivity.

3.3.2. CO_2-TPD Characterization. C2 selectivity has been reported to be correlated with the acid−base properties of catalysts.[19,53,54] We performed CO_2-TPD characterization to measure the acid−base properties of the $La_2O_2CO_3$−H and $La_2O_2CO_3$−P catalysts. As shown in Figure 6, the peak at ∼780 °C represents either the strongly basic sites over the catalysts or the decomposition of hexagonal oxycarbonates,[55] which was corroborated by the TG-DTA results shown in Figure 1 and Scheme 1. The peaks at 464 °C ($La_2O_2CO_3$−H) and 567 °C ($La_2O_2CO_3$−P) indicate moderately basic sites[56] that were involved in the desorption of chemisorbed CO_2. Because the peak area of CO_2 desorption from $La_2O_2CO_3$−P (or $La_2O_2CO_3$−H_{ref}) was significantly less than that from $La_2O_2CO_3$−H, fewer moderately basic sites were present over $La_2O_2CO_3$−P (or $La_2O_2CO_3$−H_{ref}) than over $La_2O_2CO_3$−H (Table S1 (SI)). Additionally, the C2 selectivity of OCM was approximately 50% over $La_2O_2CO_3$−H at 420−500 °C and approximately 30% over $La_2O_2CO_3$−P at 500 °C and above, whereas no C2 products were detected over $La_2O_2CO_3$−H_{ref} (Table 2). Thus, the contribution to the C2 selectivity over $La_2O_2CO_3$−H is ascribed to the moderately basic sites, which is supported by some previous reports.[2,26,27,54] These reports have suggested that the moderately basic sites are beneficial to the desorption of C2 products in the OCM.

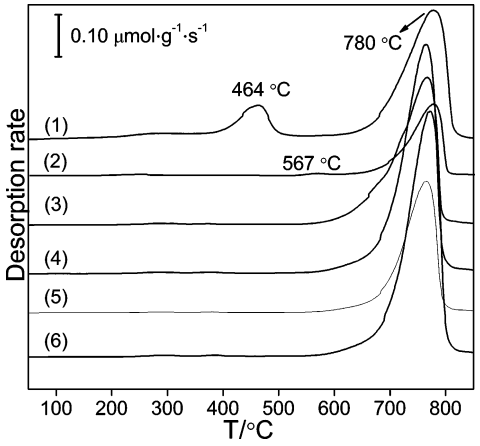

Figure 6. CO_2-TPD curves of the samples: (1) $La_2O_2CO_3$−H, (2) $La_2O_2CO_3$−P, (3) $La_2O_2CO_3$−H_{ref}, (4) La_2O_3−H, (5) La_2O_3−P, and (6) La_2O_3−H_{ref}.

Over La_2O_3−H, La_2O_3−P, and La_2O_3−H_{ref}, there are only strongly basic sites. These sites easily capture CO_2 to form carbonates, which could affect the activity and selectivity of the catalysts. For example, the La_2O_3−H sample exhibited ignition at 420 °C and generated only CO_x as products, with a 26.2% conversion of methane and a 41.5% C2 selectivity when the temperature was elevated to 450 °C. By contrast, the fresh La_2O_3−H sample demonstrated a 12.9% conversion of methane and a 25.8% C2 selectivity at 450 °C. This indicates that the carbonates formed over the sample increased the activity and C2 selectivity of the catalyst. Although significant C2 products (25.8% selectivity) were found in OCM performed over La_2O_3−H at 450 °C (Table 2), these were obviously fewer in number than the C2 products produced over $La_2O_2CO_3$−H (∼50% selectivity). This result corresponds to the fact that there are only strongly basic sites over La_2O_3−H and a great number of moderately basic sites over $La_2O_2CO_3$−H. Hence, the moderately basic sites helped to improve the C2 selectivity of OCM.

3.3.3. Comparison of $La_2O_2CO_3$ to La_2O_3. In addition to the effects of oxygen species and acid−base properties, the factors affecting the C2 selectivity of OCM include the particle sizes, specific surface areas, pore sizes, and anion radius of catalysts.[27,53,57] Although the particle size of $La_2O_2CO_3$ is almost the same as La_2O_3, $La_2O_2CO_3$ exhibited greater pore diameters, pore volume, and specific surface areas than La_2O_3 (Table 1). Furthermore, the anion (CO_3^{2-}) in $La_2O_2CO_3$ showed a larger radius than La_2O_3 and thus had a higher capacity for isolating the active sites. Thus, the dispersion of the active sites over $La_2O_2CO_3$ was better than those of La_2O_3, which could have resulted in its improved C2 selectivity in OCM. For example, there was a low density of sites for O_2 adsorption only at 200−400 °C (0.03 μmol·m^{-2}) and CO_2 adsorption at 400−600 °C (0.24 μmol·m^{-2}) over $La_2O_2CO_3$−P and no corresponding sites over La_2O_3−P (Table S1 (SI)). The O_2 and CO_2 adsorption site densities represent the amount of molecular oxygen species and

Table 3. Activity/Specific Activity of Nano $La_2O_2CO_3$ and La_2O_3 for OCM

catalysts	T/°C	conversion of methane			S_{BET}/m^2·g^{-1}
		/%	/mmol·h^{-1}·g^{-1}	/mmol·m^{-2}·h^{-1}	
$La_2O_2CO_3$−H	420	29.7	298.3	4.3	68.6
	450	30.2	303.3	4.4	
	500	30.5	306.4	4.5	
$La_2O_2CO_3$−P	420	0.0	0.0	0.0	12.2
	450	1.5	15.1	1.2	
	500	26.8	269.2	22.1	
$La_2O_2CO_3$−H_{ref}	420	0.0	0.0	0.0	71.2
	450	0.0	0.0	0.0	
	500	1.5	15.1	0.21	
La_2O_3−H	420	5.4	54.2	3.2	16.8
	450	26.2	263.2	15.7	
	500	27.4	275.2	16.4	
La_2O_3−P	450	2.3	23.1	3.9	6.0
	500	16.2	162.7	27.1	
La_2O_3−H_{ref}	450	0.0	0.0	0.0	18.0
	500	1.2	12.1	0.67	

DOI: 10.1021/cs501733r
ACS Catal. 2015, 5, 1663−1674

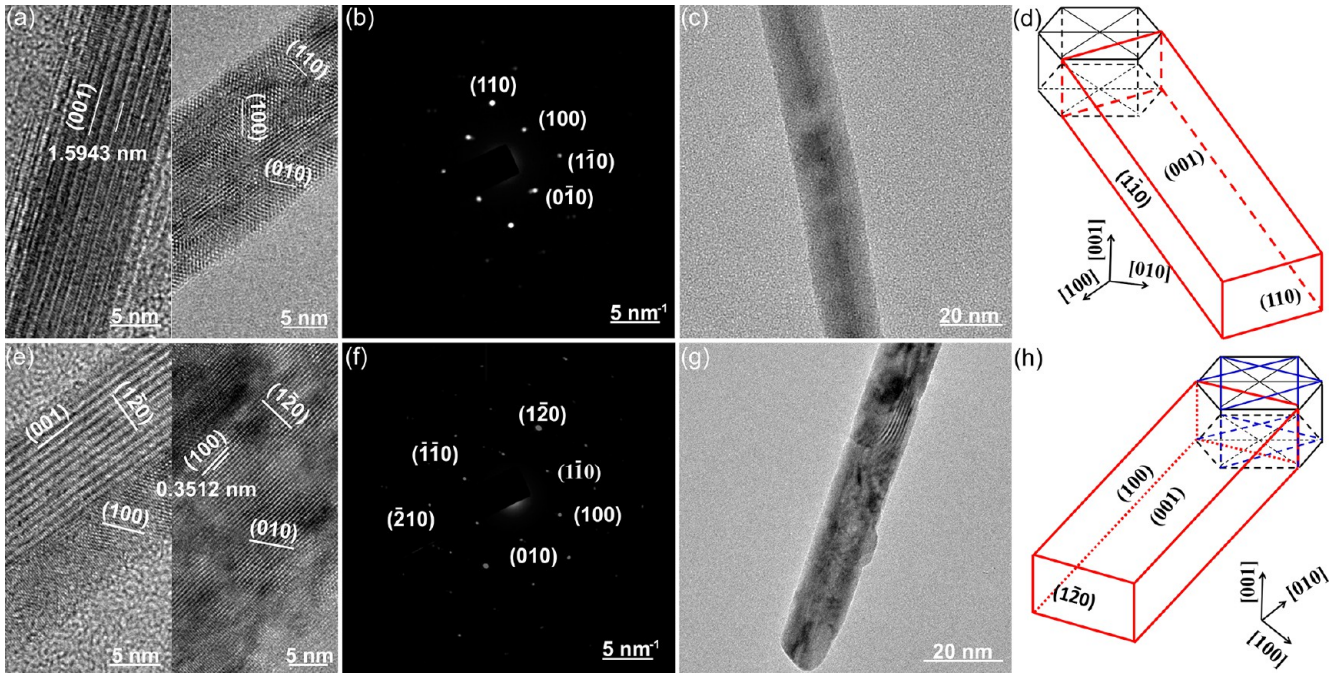

Figure 7. HRTEM, TEM images, SAED patterns and illustrations of the real shapes of $La_2O_2CO_3$–H_{ref} (a–d) and $La_2O_2CO_3$–H (e–h).

moderately basic sites over the catalyst surfaces, respectively, and almost offset each other in contributing to the C2 selectivity. However, in samples with captured CO_2, the C2 selectivity was still higher over $La_2O_2CO_3$–P (29.1%) than over La_2O_3–P (24.6%) at 500 °C and even higher than over the fresh rod-shaped La_2O_3–H sample (24.3%) at 500 °C (Table 2). Rod-shaped La_2O_3–H had a low density of sites for O_2 adsorption at 400–600 °C (0.11 μmol·m^{-2}), which was responsible for the C2 products (Table S1 (SI)). Consequently, the increased dispersion of the active sites over the catalyst could result in improvement to the reaction selectivity, which is in agreement with previous reports.[27,58,59]

Moreover, methane conversion was greater during OCM over $La_2O_2CO_3$ than during OCM over La_2O_3 because the structure of the porous $La_2O_2CO_3$ was looser than that of La_2O_3, which is related to the quantity of defects on the catalyst surfaces. For example, the initial conversion of methane during OCM over $La_2O_2CO_3$–H was ~8% at 410 °C and ~30% at 420 °C, whereas that over La_2O_3–H was ~5% at 420 °C and ~13% at 450 °C (Table 2).

Additionally, $La_2O_2CO_3$ exhibited the ability to suppress the formation of CO_x during OCM. $La_2O_2CO_3$–H exhibited ~50% C2 and ~50% CO_x selectivity during OCM at 450–500 °C, but fresh La_2O_3–H exhibited ~25% C2 and ~75% CO_x selectivity (Table 2). Therefore, the catalytic activity and selectivity were higher over $La_2O_2CO_3$ than over La_2O_3 during OCM, especially at lower temperatures (e.g., below 500 °C).

3.4. Structure Sensitivity of $La_2O_2CO_3$ and La_2O_3. As previously mentioned, at lower temperatures, the catalytic activity of the rod-shaped $La_2O_2CO_3$–H for OCM is greater than that of the plate-shaped $La_2O_2CO_3$–P. However, the specific surface area of $La_2O_2CO_3$–H is ~5 times larger than that of $La_2O_2CO_3$–P; thus, the specific activity of $La_2O_2CO_3$–H for OCM is higher at 420–450 °C and lower at 500 °C relative to the specific activity of $La_2O_2CO_3$–P (Table 3). Similar statements can be made for the comparison of $La_2O_2CO_3$ with La_2O_3. For example, the specific activity of La_2O_3–H is higher than that of $La_2O_2CO_3$–H at 450 °C and above. This result reveals that the number of active sites on the catalysts' surfaces is less important for OCM after the reaction is ignited at an adequately high temperature.

Additionally, Sun and co-workers[2] recently reported that La_2O_3 nanorods exhibited greater catalytic performances for OCM than La_2O_3 nanoparticles at 650 °C and below, being indicative of shape effects of La_2O_3 nanocatalysts for OCM. Likewise, our results show that, for OCM at 420–500 °C, the conversion of methane over the rod-shaped La_2O_3–H is significantly higher than that over the plate-shaped La_2O_3–P (Table 3), but the specific activity of La_2O_3–H is lower than that of La_2O_3–P at 500 °C and above if the specific surface area is considered.

To investigate the effects of the structure of the rod-shaped sample $La_2O_2CO_3$–H on OCM, we take the rod-shaped sample $La_2O_2CO_3$–H_{ref} (with a specific surface area similar to that of $La_2O_2CO_3$–H) as the reference catalyst. As shown in Table 3, the conversion of methane over $La_2O_2CO_3$–H_{ref} was far lower than that over $La_2O_2CO_3$–H at lower temperatures (below 500 °C). The specific activities of $La_2O_2CO_3$–H_{ref} and $La_2O_2CO_3$–H for methane oxidation were 0.21 and 4.5 mmol·m^{-2}·h^{-1} at 500 °C, respectively. The latter is ~20 times greater than the former.

Moreover, the O_2-TPD profiles illustrate that the $La_2O_2CO_3$–H_{ref} differs substantially from $La_2O_2CO_3$–H. As shown in Figure 5, two oxygen species are desorbed from $La_2O_2CO_3$–H, whereas no oxygen is desorbed from $La_2O_2CO_3$–H_{ref}. The peak area of oxygen desorption from $La_2O_2CO_3$–H is far larger than that from $La_2O_2CO_3$–H_{ref}, indicating that $La_2O_2CO_3$–H has a much higher OSC than $La_2O_2CO_3$–H_{ref} (see also Table S1 (SI)).

Furthermore, CO_2-TPD profiles show that $La_2O_2CO_3$–H adsorbs more CO_2 than does $La_2O_2CO_3$–H_{ref} (Figure 6, Table S1 (SI)). The peak at 464 °C for $La_2O_2CO_3$–H is attributed to desorption of the chemisorbed CO_2, and the peak at 780 °C for $La_2O_2CO_3$–H and $La_2O_2CO_3$–H_{ref} is assigned to the decomposition of the oxycarbonates.

DOI: 10.1021/cs501733r
ACS Catal. 2015, 5, 1663–1674

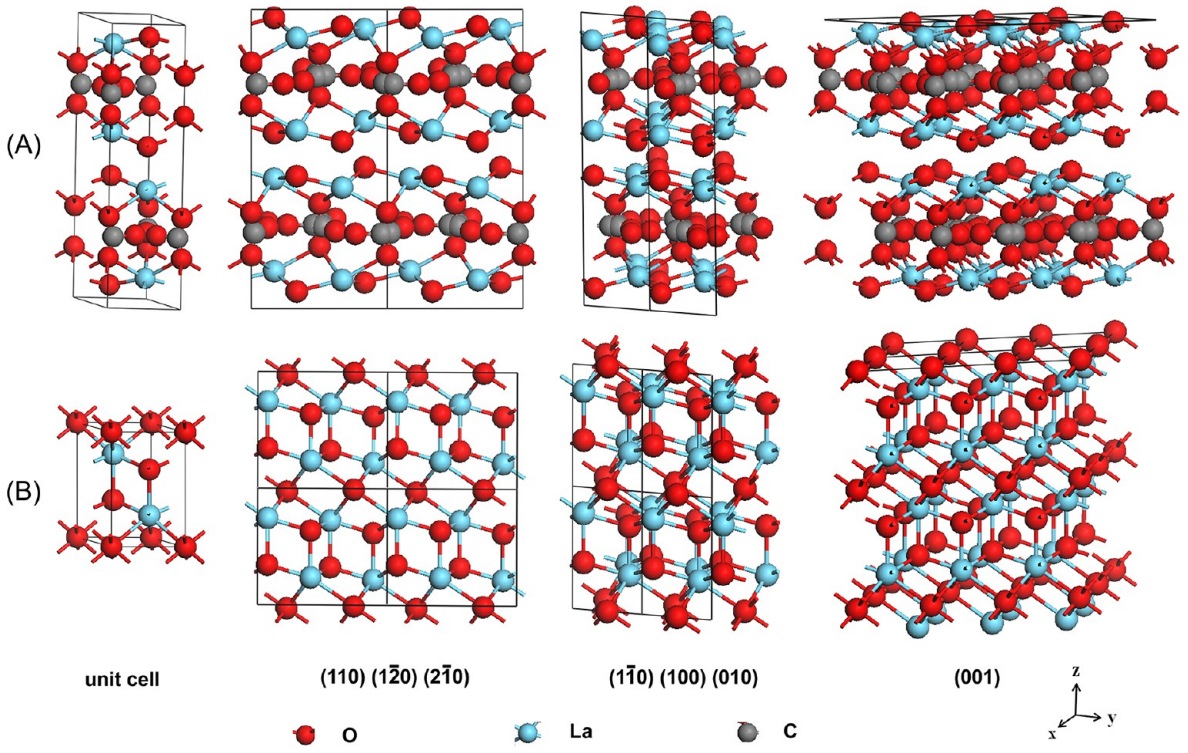

Figure 8. Unit cell of the hexagonal-structured $La_2O_2CO_3$ (A) and La_2O_3 (B) crystals and the surface atomic configurations of their (110), (1$\bar{2}$0), (2$\bar{1}$0), (100), (010), (1$\bar{1}$0), and (001) planes.

Although both $La_2O_2CO_3$−H and $La_2O_2CO_3$−H_{ref} nanoparticles are rod-shaped, and their specific surface areas and pore parameters are very similar to each other (Table 1), they exhibit substantially different behavior in the activation of methane and in the adsorption of oxygen and carbon dioxide.

In Figure 7 are shown TEM images and SAED patterns of the $La_2O_2CO_3$−H_{ref} and $La_2O_2CO_3$−H samples. The rod-shaped sample $La_2O_2CO_3$−H_{ref} is indexed to a phase with a hexagonal structure grown along the [110] direction, which is consistent with the results reported by Shen.[30] On the basis of the HRTEM, TEM images and the SAED patterns of $La_2O_2CO_3$−H_{ref} (Figure 7a−c), the rod-shaped sample $La_2O_2CO_3$−H_{ref} was determined to be mainly enclosed by two (1$\bar{1}$0) side planes, two (001) flat planes and two (110) end planes, along with (100) and (010) planes (see Figure 7d). Similarly, the rod-shaped sample $La_2O_2CO_3$−H, which has a hexagonal structure grown along the [010] direction (or [1$\bar{2}$0] by reciprocal lattice), was observed to be principally enclosed by two (100) side planes, two (001) flat planes and two (1$\bar{2}$0) end planes, along with the planes (010), (1$\bar{1}$0), (110) and (2$\bar{1}$0) (see Figure 7h) (cf. the exposed facet of the plate-shaped sample $La_2O_2CO_3$−P is (100), Figure S4 (SI)). In the latter case, two (2$\bar{1}$0) planes and two (110) planes lean toward the (100) side planes more than the planes (010) and (1$\bar{1}$0), meaning that they have a larger ratio in the exposed facets of the nanorod than the (010) and (1$\bar{1}$0) planes and the (1$\bar{2}$0) end planes. Hence, the behavior differences between $La_2O_2CO_3$−H and $La_2O_2CO_3$−H_{ref} are related to their exposed facets.

According to the reported crystallographic data,[60] each La^{3+} cation in a $La_2O_2CO_3$ crystal is surrounded by seven oxygen anions: four exist in tetrahedral coordination and three are in octahedral coordination (lattice parameters: a = 4.0755 Å, b = 4.0755 Å, c = 15.9570 Å, α = 90°, β = 90°, and γ = 120°). Using the unit cell model (Figure 8A), we calculated the atomic densities of oxygen, lanthanum, and carbon (ρ_{O1}, ρ_O, ρ_{La}, ρ_C) on the crystal planes (Table 4). Notably, the atomic densities (ρ_{O1}, ρ_O, ρ_{La}, ρ_C) on the exposed facets followed the order (001) > (100)(1$\bar{1}$0)(010) > (110)(1$\bar{2}$0)(2$\bar{1}$0), that is, the atomic densities were much lower on the (110), (1$\bar{2}$0), and (2$\bar{1}$0) facets than on the other facets. Because the $La_2O_2CO_3$−H sample had a large ratio of exposed (2$\bar{1}$0) and (110) facets with low atomic densities, its structure was determined to be loose, unlike the $La_2O_2CO_3$−H_{ref} sample. Furthermore, the ratio of O to La was lower on the exposed facets with low atomic densities than on the exposed facets with high atomic densities (Table 4). According to the surface atomic composition determined by XPS analysis, the ratio of O to La on the $La_2O_2CO_3$−H surface was less than that of $La_2O_2CO_3$−H_{ref} (Table S3 (SI)), suggesting that the atomic densities on the $La_2O_2CO_3$−H surface were lower. This result is consistent with our calculated results. In addition, the nearest coordination number of La in $La_2O_2CO_3$ was 4 for the exposed (1$\bar{2}$0), (2$\bar{1}$0) and (110) facets, 5 for the (100), (010) and (1$\bar{1}$0) facets, and 6 for the (001) facets (Figure 8A). These coordination numbers reveal that the atomic coordination was much less saturated for $La_2O_2CO_3$−H than for $La_2O_2CO_3$−H_{ref}

Table 4. Atomic Densities on Crystal Planes

atom[a]	atomic density (ρ) on crystal planes/Å^{-2}		
	(110) (1$\bar{2}$0) (2$\bar{1}$0)	(100)(010) (1$\bar{1}$0)	(001)
O_1	0.04	0.06	0.07
O	0.08	0.23	1.81
La	0.03	0.09	0.28
C	0.03	0.08	0.42

[a]O_1 stands for oxygen atom on the surface; O, La, and C stand for oxygen, lanthanum, and carbon atom (near the surface) in the unit cell of the crystal.

DOI: 10.1021/cs501733r
ACS Catal. 2015, 5, 1663−1674

and that some vacancies or defects were available on the surfaces (see Figure 7e,g). These vacancies are beneficial to the adsorption and activation of methane and oxygen. Thus, $La_2O_2CO_3$−H with exposed (110), (1$\bar{2}$0) and (2$\bar{1}$0) facets with low atomic densities exhibited a stronger ability to adsorb and activate methane and oxygen compared to $La_2O_2CO_3$−H_{ref}. This result is in good agreement with the results of the tests of the catalytic properties and the O_2-TPD results (Table 3, Figure 5).

The rod-shaped and plate-shaped La_2O_3 nanoparticles obtained from the thermal decomposition of either the rod-shaped and plate-shaped samples of $La_2O_2CO_3$ or $La(OH)_3$ calcined in air at 700 °C exhibited the same morphology as $La_2O_2CO_3$. Moreover, the catalytic properties of rod-shaped and plate-shaped La_2O_3 nanoparticles were similar to those of $La_2O_2CO_3$. For instance, the La_2O_3−H sample exhibited ∼24 times greater specific activity toward methane oxidation compared to La_2O_3−H_{ref} at 500 °C (Table 3). At low temperatures (400−600 °C), La_2O_3−H adsorbed more oxygen than La_2O_3−H_{ref} and La_2O_3−P (0.11 vs 0 μmol·m^{-2}, Table S1 (SI)). These results are related to the structures of the catalyst surfaces.

The HRTEM images and SAED patterns of La_2O_3−H and La_2O_3−H_{ref} are shown in Figure S5 (SI). The exposed crystalline planes were the same for these samples as for the corresponding $La_2O_2CO_3$ sample. Thus, La_2O_3 also exhibited the same structure sensitivity in the OCM at lower temperatures (500 °C and below).

To explore the changes of surface structures from the decomposition of $La_2O_2CO_3$−H into La_2O_3−H, we compared the structures of their exposed planes. As shown in Figure 8, the atomic configurations on the exposed facets of La_2O_3 were similar to those of $La_2O_2CO_3$, revealing that La_2O_3−H produced by the decomposition of $La_2O_2CO_3$−H and the removal of CO_2 can well maintain the skeleton of the La and O atoms. More interestingly, when $La_2O_2CO_3$−H was prepared via the dissolution of La_2O_3−H in water followed by desiccation and calcination, the sample exhibited slightly lower catalytic performance for OCM compared to the initial $La_2O_2CO_3$−H (Table 2). This small difference was caused by the presence of a small amount of remaining La_2O_3−H; that is, La_2O_3−H was not fully hydrolyzed into $La(OH)_3$−H (Figures S6 and S7 (SI)), as suggested by the diminished peak at 30.1° in Figure S6 (SI), indicating the presence of La_2O_3. Thus, the $La_2O_2CO_3$−H obtained from the water-treated La_2O_3−H was mixed with a small quantity of La_2O_3, resulting in subtle changes to its catalytic performance. Hence, the structure of the rod-shaped La_2O_3−H nanoparticles is not significantly different from that of $La_2O_2CO_3$−H, which is the reason why the rod-shaped La_2O_3−H exhibited good catalytic performance in the OCM carried out at low temperatures.

3.5. Stability of $La_2O_2CO_3$ in the OCM. Nanosized metal oxide samples with loose structures and well-defined morphologies are commonly unstable and are reconstructed easily in reactions, especially during alkane oxidation. Figure 9 shows the catalytic performances over the $La_2O_2CO_3$−H catalyst as the time-on-stream under conditions of T = 500 °C, CH_4/O_2 = 3/1 (molar ratio), and GHSV = 30 000 mL·g^{-1}·h^{-1}. Both the methane conversion and C2 selectivity were observed to be almost unchanged over 3000 min (50 h) of time-on-stream. This finding was supported by the characterization results of the catalyst after the reaction. The S(T)EM images and the XRD and SAED patterns indicated that the XRD peaks and morphologies did not change substantially over the course of the OCM reaction

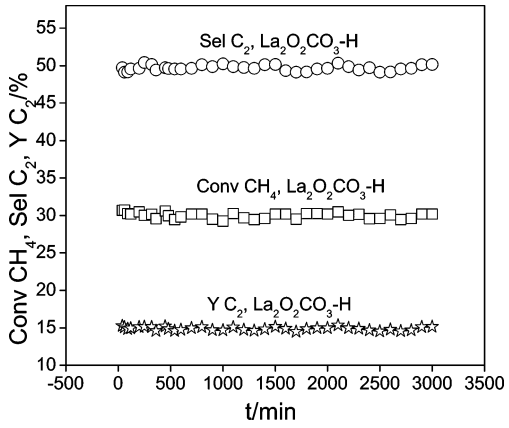

Figure 9. Methane conversion (Conv), C2 selectivity (Sel), and C2 yield (Y) with time-on-stream over $La_2O_2CO_3$−H. Reaction conditions: 500 °C; GHSV = 30 000 mL·g^{-1}·h^{-1}; CH_4/O_2 = 3/1 molar ratio.

for 3000 min (Figure 10−12). Thus, the $La_2O_2CO_3$−H catalyst is stable under OCM conditions.

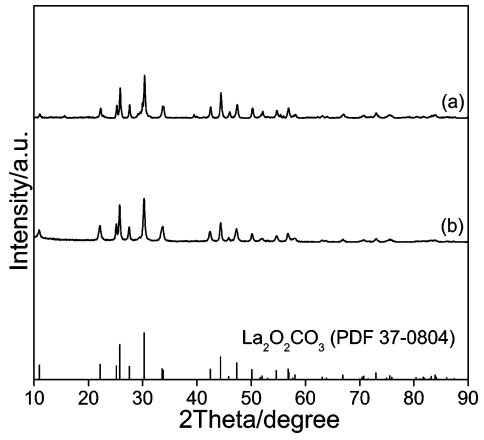

Figure 10. XRD patterns of $La_2O_2CO_3$−H before (a) and after (b) OCM for 3000 min.

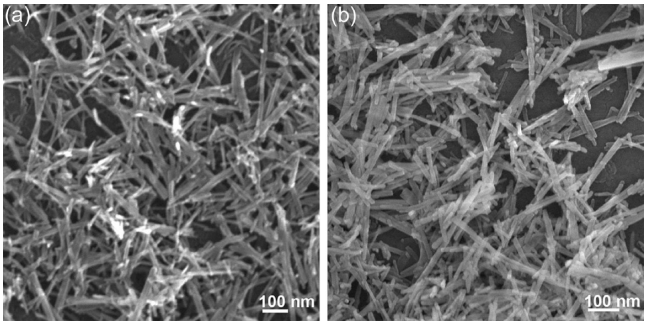

Figure 11. SEM images of $La_2O_2CO_3$−H before (a) and after (b) OCM for 3000 min.

4. CONCLUDING REMARKS

Based on the previous discussion, we drew several main conclusions.

Nanoscale $La_2O_2CO_3$ samples with different morphologies (rod- and plate-shape) were synthesized. Though the particle sizes of the rod-shaped and plate-shaped samples were approximately the same, the structure of the rod-shaped sample

DOI: 10.1021/cs501733r
ACS Catal. 2015, 5, 1663−1674

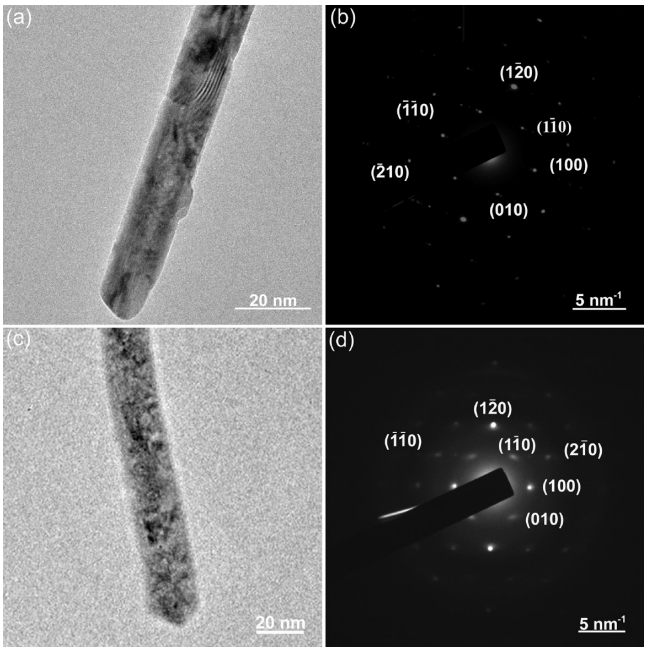

Figure 12. TEM (a, c) images and SAED (b, d) patterns of $La_2O_2CO_3$−H before (a, b) and after (c, d) OCM for 3000 min.

was looser than that of the plate-shaped sample, and the specific surface area and pore parameters (pore diameters, pore volume) of the rod-shaped sample were larger than those of the plate-shaped sample.

The methane oxidation reaction was ignited over the plate-shaped sample $La_2O_2CO_3$−P at 440 °C, and the C2 products were only detected at 500 °C and above. The reaction was ignited over the rod-shaped sample $La_2O_2CO_3$−H at 410 °C, and the C2 products with a selectivity of ∼50% were formed at 420 °C and above. The rod-shaped $La_2O_2CO_3$−H is a superior catalyst in the OCM compared to the plate-shaped $La_2O_2CO_3$−P, especially at lower temperatures (below 500 °C). These results suggest that this difference in catalytic performance is related to the catalysts' different morphologies.

Furthermore, the methane oxidation reaction was ignited over the rod-shaped $La_2O_2CO_3$−H_{ref} sample at 500 °C, without the formation of C2 products. The rod-shaped $La_2O_2CO_3$−H_{ref} sample was an inferior catalyst in the OCM relative to the rod-shaped $La_2O_2CO_3$−H sample, even though the specific surface areas and the pore parameters of the two samples were very similar. The specific activity of $La_2O_2CO_3$−H was 20 times greater than that of $La_2O_2CO_3$−H_{ref}.

The O_2-TPD and CO_2-TPD characterizations showed that $La_2O_2CO_3$−H exhibited a larger capacity for oxygen and CO_2 adsorption compared to $La_2O_2CO_3$−P and $La_2O_2CO_3$−H_{ref}. Moreover, $La_2O_2CO_3$−H could facilitate the formation of the chemisorbed oxygen species and moderately basic sites. The dispersions of the active sites, the chemisorbed oxygen species and the moderately basic sites over the catalysts were beneficial to the formation of C2 products, and the formation of molecular oxygen species was related to the complete oxidation of methane.

From the TEM images and the SAED and XRD patterns, we determined that the $La_2O_2CO_3$−H sample was enclosed by the (100)(side), (001)(flat), (1$\bar{2}$0)(end), (010), (1$\bar{1}$0), (2$\bar{1}$0) and (110) planes. The $La_2O_2CO_3$−H_{ref} sample was enclosed by the (1$\bar{1}$0) (side), (001)(flat), (110)(end), (100) and (010) facets. In particular, the (110) and (2$\bar{1}$0) planes of $La_2O_2CO_3$−H were inclined toward the (100) side plane, with good ratios between the exposed facets. The atomic configuration on the (110), (2$\bar{1}$0) and (1$\bar{2}$0) facets was far looser than that of the other exposed facets; thus, the structure of the $La_2O_2CO_3$−H sample was looser than that of the $La_2O_2CO_3$−H_{ref} sample. Therefore, the behavioral differences between $La_2O_2CO_3$−H and $La_2O_2CO_3$−H_{ref} arose from differences in their exposed facets.

Similar conclusions were made for La_2O_3−H, La_2O_3−P and La_2O_3−H_{ref}. The exposed facets of these samples were the same as the corresponding $La_2O_2CO_3$ facets, and, like $La_2O_2CO_3$, La_2O_3 exhibited significant structure sensitivity to OCM. However, the catalytic properties of La_2O_3 were lower than those of $La_2O_2CO_3$, which has the ability to suppress CO_x formation.

Finally, $La_2O_2CO_3$−H was more stable than La_2O_3 in the OCM. $La_2O_2CO_3$−H maintained good stability for the tested 3000 min of OCM, and its structure was well maintained during the reaction.

■ ASSOCIATED CONTENT

Supporting Information

The following file is available free of charge on the ACS Publications website at DOI: 10.1021/cs501733r.

TPD-MS studies of the thermal decomposition of $La(OH)_3$; particle size distributions of the samples; (HR)TEM images and XRD patterns of $La_2O_2CO_3$−P; HRTEM images and SAED patterns of La_2O_3−H and La_2O_3−H_{ref}; HRTEM images of La_2O_3−P; XPS spectra of $La_2O_2CO_3$; analysis of the surface atomic composition; the density of sites for O_2 and CO_2 adsorption; and the XRD patterns and SEM images of $La(OH)_3$-H and water-treated La_2O_3−H (PDF)

■ AUTHOR INFORMATION

Corresponding Authors

*E-mail: wsxia@xmu.edu.cn.

*E-mail: hlwan@xmu.edu.cn.

Author Contributions

All authors have given approval to the final version of the manuscript.

Notes

The authors declare no competing financial interest.

■ ACKNOWLEDGMENTS

Support for this research from the Ministry of Science and Technology of China (2010CB732303), the National Natural Science Foundation of China (21373169, 21033006), NFFTBS (No. J1310024), and the Program for Changjiang Scholars, and the Innovative Research Team at the University (No. IRT_14R31) is gratefully acknowledged.

■ REFERENCES

(1) Feng, X.; Duan, X. Z.; Qian, G.; Zhou, X. G.; Chen, D.; Yuan, W. K. *J. Catal.* **2014**, *317*, 99−104.

(2) Huang, P.; Zhao, Y. H.; Zhang, J.; Zhu, Y.; Sun, Y. H. *Nanoscale* **2013**, *5*, 10844−10848.

(3) Zhao, Y.; Ma, W.; Li, Y.; Ji, H.; Chen, C.; Zhu, H.; Zhao, J. *Angew. Chem., Int. Ed.* **2012**, *51*, 3188−3192.

(4) Fischer, N.; van Steen, E.; Claeys, M. *Catal. Today* **2011**, *171*, 174−179.

(5) Zhang, H.; Jin, M. S.; Xiong, Y. J.; Lim, B. K.; Xia, Y. N. *Acc. Chem. Res.* **2013**, *46*, 1783−1794.

DOI: 10.1021/cs501733r
ACS Catal. 2015, 5, 1663−1674

(6) Krcha, M. D.; Mayernick, A. D.; Janik, M. J. *J. Catal.* **2012**, *293*, 103−115.
(7) Spencer, N. D.; Schoonmaker, R. C.; Somorjai, G. A. *Nature* **1981**, *294*, 643−644.
(8) Tian, N.; Zhou, Z. Y.; Sun, S. G.; Ding, Y.; Wang, Z. L. *Science* **2007**, *316*, 732−735.
(9) Schmidt, E.; Vargas, A.; Mallat, T.; Baiker, A. *J. Am. Chem. Soc.* **2009**, *131*, 12358−12367.
(10) Ziółkowski, J. *J. Catal.* **1983**, *80*, 263−273.
(11) Singhania, N.; Anumol, E. A.; Ravishankar, N.; Madras, G. *Dalton Trans.* **2013**, *42*, 15343−15354.
(12) Zhou, K. B.; Wang, X.; Sun, X. M.; Peng, Q.; Li, Y. D. *J. Catal.* **2005**, *229*, 206−212.
(13) Mai, H. X.; Sun, L. D.; Zhang, Y. W.; Si, R.; Feng, W.; Zhang, H. P.; Liu, H. C.; Yan, C. H. *J. Phys. Chem. B* **2005**, *109*, 24380−24385.
(14) Tana; Zhang, M. L.; Li, J.; Li, H. J.; Li, Y.; Shen, W. J. *Catal. Today* **2009**, *148*, 179−183.
(15) Hou, Y. H.; Chang, G.; Weng, W. Z.; Xia, W. S.; Wan, H. L. *Chin. J. Catal.* **2011**, *32*, 1531−1536.
(16) Wang, J. X.; Chou, L. J.; Zhang, B.; Song, H. L.; Yang, J.; Zhao, J.; Li, S. B. *Catal. Comm.* **2006**, *7*, 59−63.
(17) Fallah, B.; Falamaki, C. *AIChE J.* **2010**, *56*, 717−728.
(18) Gao, Z. M.; Shi, Y. X. *J. Nat. Gas Chem.* **2010**, *19*, 173−178.
(19) Dedov, A. G.; Nipan, G. D.; Loktev, A. S.; Tyunyaev, A. A.; Ketsko, V. A.; Parkhomenko, K. V.; Moiseev, I. I. *Appl. Catal., A* **2011**, *406*, 1−12.
(20) Derk, A.; Moore, G.; Sharma, S.; McFarland, E.; Metiu, H. *Top. Catal.* **2014**, *57*, 118−124.
(21) Noon, D.; Seubsai, A.; Senkan, S. *ChemCatChem.* **2013**, *5*, 146−149.
(22) Ferreira, V.; Tavares, P.; Figueiredo, J.; Faria, J. *Catal. Comm.* **2013**, *42*, 50−53.
(23) Zhang, X. H.; Yi, X. D.; Zhang, J. W.; Xie, Z. X.; Kang, J. Y.; Zheng, L. S. *Inorg. Chem.* **2010**, *33*, 10244−10246.
(24) Sekine, Y.; Tanaka, K.; Matsukata, M.; Kikuchi, E. *Energy Fuel.* **2009**, *23*, 613−616.
(25) Rane, V. H.; Chaudhari, S. T.; Choudhary, V. R. *J. Nat. Gas Chem.* **2010**, *19*, 25−30.
(26) Dedov, A. G.; Loktev, A. S.; Moiseev, I. I.; Aboukais, A.; Lamonier, J. F.; Filimonov, I. N. *Appl. Catal., A* **2003**, *245*, 209−220.
(27) Hou, Y. H.; Lin, Y. L.; Li, Q.; Weng, W. Z.; Xia, W. S.; Wan, H. L. *ChemCatChem.* **2013**, *5*, 3725−3735.
(28) Taylor, R. P.; Schrader, G. L. *Ind. Eng. Chem. Res.* **1991**, *30*, 1016−1023.
(29) Au, C. T.; He, H.; Lai, S. Y.; Ng, C. F. *J. Catal.* **1996**, *163*, 399−408.
(30) Wang, F.; Shi, R. J.; Liu, Z. Q.; Shang, P. J.; Pang, X.; Shen, S.; Feng, Z. C.; Li, C.; Shen, W. J. *ACS Catal.* **2013**, *3*, 890−894.
(31) Bernal, S.; Díaz, J. A.; García, R.; Rodríguez-Izquierdo, J. M. *J. Mater. Sci.* **1985**, *20*, 537−541.
(32) Bernal, S.; Botana, F. J.; Garcia, R.; Ramirez, F.; Rodríguez-Izquierdo, J. M. *J. Mater. Sci.* **1987**, *22*, 3793−3800.
(33) Mu, Q. Y.; Chen, T.; Wang, Y. D. *Nanotechnology* **2009**, *20*, 345602.
(34) Mu, Q. Y.; Wang, Y. D. *J. Alloy. Compd.* **2011**, *509*, 396−401.
(35) Caro, P. E.; Sawyer, J. O.; Evning, L. *Spectrochim. Acta, Part A* **1972**, *28*, 1167−1173.
(36) Rosynek, M. P.; Magnuson, D. T. *J. Catal.* **1977**, *46*, 402−413.
(37) Zubova, N.; Makarov, V.; Nikolskii, V.; Petrov, P.; Teterin, E.; Chebotarev, N. *Russ. J. Inorg. Chem.* **1968**, *13*, 7−15.
(38) Levan, T.; Che, M.; Tatibouet, J. M.; Kermarec, M. *J. Catal.* **1993**, *142*, 18−26.
(39) Aghazadeh, M.; Arhami, B.; Malek Barmi, A.-A.; Hosseinifard, M.; Gharailou, D.; Fathollahi, F. *Mater. Lett.* **2014**, *115*, 68−71.
(40) Spinicci, R.; Tofanari, A. *Catal. Today* **1990**, *6*, 473−479.
(41) Wang, J. X.; Lunsford, J. H. *J. Phys. Chem.* **1986**, *90*, 3890−3891.
(42) Kalenik, Z.; Wolf, E. E. *Catal. Today* **1992**, *13*, 255−264.
(43) Xia, W. S.; Li, J. H.; Weng, W. Z.; Wan, H. L. *Chem. Phys. Lett.* **2006**, *423*, 427−433.
(44) Kazansky, V. B. *Kinet. Katal.* **1977**, *18*, 43−54.
(45) Shvets, V.; Vrotyntsev, V.; Kazansky, V. *Kinet. Katal.* **1969**, *10*, 356−363.
(46) Xia, W. S.; Zhang, D.; Weng, W. Z.; Wan, H. L. *Chin. J. Catal.* **2013**, *34*, 2130−2137.
(47) Ding, W. P.; Chen, Y.; Fu, X. C. *Catal. Lett.* **1994**, *23*, 69−78.
(48) Ding, W. P.; Chen, Y.; Fu, X. C. *Appl. Catal., A* **1993**, *104*, 61−75.
(49) Zhang, X.; He, D. H.; Zhang, Q. J.; Xu, B. Q.; Zhu, Q. M. *Top. Catal.* **2005**, *32*, 215−223.
(50) Gopinath, C. S.; Hegde, S. G.; Ramaswamy, A. V.; Mahapatra, S. *Mater. Res. Bull.* **2002**, *37*, 1323−1332.
(51) Rodriguez, J. A.; Hrbek, J.; Kuhn, M.; Sham, T. K. *J. Phys. Chem.* **1993**, *97*, 4737−4744.
(52) Peng, X. D.; Richards, D. A.; Stair, P. C. *J. Catal.* **1990**, *121*, 99−109.
(53) Rane, W. H.; Chaudhari, S. T.; Choudhary, V. R. *J. Chem. Technol. Biot.* **2006**, *81*, 208−215.
(54) Papa, F.; Luminita, P.; Osiceanu, P.; Birjega, R.; Akane, M.; Balint, I. *J. Mol. Catal. A* **2011**, *346*, 46−54.
(55) Xin, S. M.; Wang, L. G.; Li, H. Q.; Huang, K. L.; Li, F. J. *Fuel Process. Technol.* **2014**, *126*, 453−459.
(56) Kim, J. T.; Anderson, J. L. *Ind. Eng. Chem. Res.* **1991**, *30*, 1008−1016.
(57) Hou, S. C.; Cao, Y.; Xiong, W.; Liu, H. C.; Kou, Y. *Ind. Eng. Chem. Res.* **2006**, *45*, 7077−7083.
(58) Ligthart, D. A. J. M.; van Santen, R. A.; Hensen, E. J. M. *J. Catal.* **2011**, *280*, 206−220.
(59) Grasselli, R. *Top. Catal.* **2002**, *21*, 79−88.
(60) Olafsen, A.; Larsson, A. K.; Fjellvåg, H.; Hauback, B. C. *J. Solid State Chem.* **2001**, *158*, 14−24.

DOI: 10.1021/cs501733r
ACS Catal. 2015, 5, 1663−1674